

CLIMATOLOGY

Anthropogenic forcing has increased the risk of longer-traveling and slower-moving large contiguous heatwaves

Ming Luo^{1,2,*†}, Sijia Wu^{1†}, Gabriel Ngar-Cheung Lau³, Tao Pei^{4*}, Zhen Liu⁵, Xiaoyu Wang¹, Guicai Ning⁶, Ting On Chan¹, Yuanjian Yang⁶, Wei Zhang^{7*}

Heatwaves are consecutive hot days with devastating impacts on human health and the environment. These events may evolve across both space and time, characterizing a spatiotemporally contiguous propagation pattern that has not been fully understood. Here, we track the spatiotemporally contiguous heatwaves in both reanalysis datasets and model simulations and examine their moving patterns (i.e., moving distance, speed, and direction) in different continents and periods. Substantial changes in contiguous heatwaves have been identified from 1979 to 2020, with longer persistence, longer traveling distance, and slower propagation. These changes have been amplified since 1997, probably due to the weakening of eddy kinetic energy, zonal wind, and anthropogenic forcing. The results suggest that longer-lived, longer-traveling, and slower-moving contiguous heatwaves will cause more devastating impacts on human health and the environment in the future if greenhouse gas emissions keep rising and no effective measures are taken immediately. Our findings provide important implications for the adaptation and mitigation of globally connected extreme heatwaves.

INTRODUCTION

Heatwaves with prolonged and consecutive periods of excessive heat have caused detrimental impacts on human health (1), economy (2, 3), agriculture (4), labor productivity (5), wildfires (6), etc. For example, a record-breaking heatwave event that occurred across Europe in 2003 caused huge socioeconomic losses and ~70,000 excess deaths (7, 8). Under global warming, heatwaves have increased in frequency, intensity, and duration notably across many parts of the world during the past decades (9). Moreover, these metrics are projected to further intensify in the coming decades under different carbon dioxide emission and socioeconomic development scenarios (10–12). Considering that heatwaves travel jointly in space and time (hereafter, spatiotemporally contiguous heatwaves), an understanding of their spatiotemporal evolution and/or propagation behavior is needed for mitigating the impacts caused by heatwaves (9, 13–15). Figure 1A provides an example of the spatiotemporal structure of a contiguous heatwave event occurring from 31 May to 17 June 1997, which started as a small event over the Middle East on 31 May, propagated eastward, and reached northeastern Asia on 17 June.

Previous studies have examined the behavior of heatwaves in terms of frequency, intensity, duration, and spatial extent (16, 17). For example, Keellings *et al.* (18) have examined the size and shape of heatwave in North America. Lyon *et al.* (13) have investigated the

spatial extent of contiguous heatwaves in the United States and found the increasing extent of these events under the Representative Concentration Pathway 8.5 (RCP 8.5) scenario. Rogers *et al.* (19) have focused on the concurrent large heatwaves in the Northern Hemisphere and indicated that these events become more frequent and severe. However, these studies mainly examined either the temporal changes of heatwaves at fixed stations (or grid points) or the spatial variation over a fixed duration. This gap hinders a comprehensive understanding of how contiguous heatwave events dynamically evolve in both space and time. While several studies have studied the magnitude, spatial extent, and duration of the connected heatwaves in space-time dimension (9, 15), these studies did not examine the moving patterns of contiguous heatwaves, such as their moving distance, moving speed, and moving direction. Only few region-scale studies have examined the moving characteristics of contiguous heatwaves (20), a globe-wide assessment is lacking, and the role of anthropogenic forcings in large contiguous heatwaves at a global scale has not been revealed.

Here, we assess the heatwave behaviors by additional metrics in addition to frequency, duration, and magnitude, that is, evolution and/or propagation. Albeit the importance of these metrics for heatwave propagation and early warning, they are difficult to define and remain largely unexplored, especially at global scale. Characterizing the propagation information of heatwaves under anthropogenic climate warming can improve our understanding of their regular movement patterns, which can serve as more criteria to track the entire lifecycles of heatwaves and thus provide potential implications for early forecasting and prediction.

RESULTS AND DISCUSSION

Mean state of contiguous heatwaves

We focus on the large contiguous heatwaves with the accumulated area (the sum of the areal extent of all grid cells across all days of the event; see Table 1) ≥ 1 million km² in the global land regions. The spatial distribution of the centroids of the entire large contiguous

Copyright © 2024 The Authors, some rights reserved; exclusive licensee American Association for the Advancement of Science. No claim to original U.S. Government Works. Distributed under a Creative Commons Attribution NonCommercial License 4.0 (CC BY-NC).

¹Guangdong Provincial Key Laboratory of Urbanization and Geo-simulation, School of Geography and Planning, Sun Yat-sen University, Guangzhou 510006, China. ²Institute of Environment, Energy, and Sustainability, The Chinese University of Hong Kong, Hong Kong, SAR, China. ³Program in Atmospheric and Oceanic Sciences, Princeton University, Princeton, NJ 08540-6654, USA. ⁴State Key Laboratory of Resources and Environmental Information System, Institute of Geographic Sciences and Natural Resources Research, Chinese Academy of Sciences, Beijing 100101, China. ⁵Earth, Ocean, and Atmospheric Sciences (EOAS) Thrust, Function Hub, The Hong Kong University of Science and Technology (Guangzhou), Guangzhou, China. ⁶School of Atmospheric Physics, Nanjing University of Information Science & Technology, Nanjing 210044, China. ⁷Department of Plants, Soils, and Climate, Utah State University, Logan, UT 84322-4820, USA.

*Corresponding author. Email: luom38@mail.sysu.edu.cn (M.L.); w.zhang@usu.edu (W.Z.); peit@reis.ac.cn (T.P.)

†These authors contributed equally to this work.

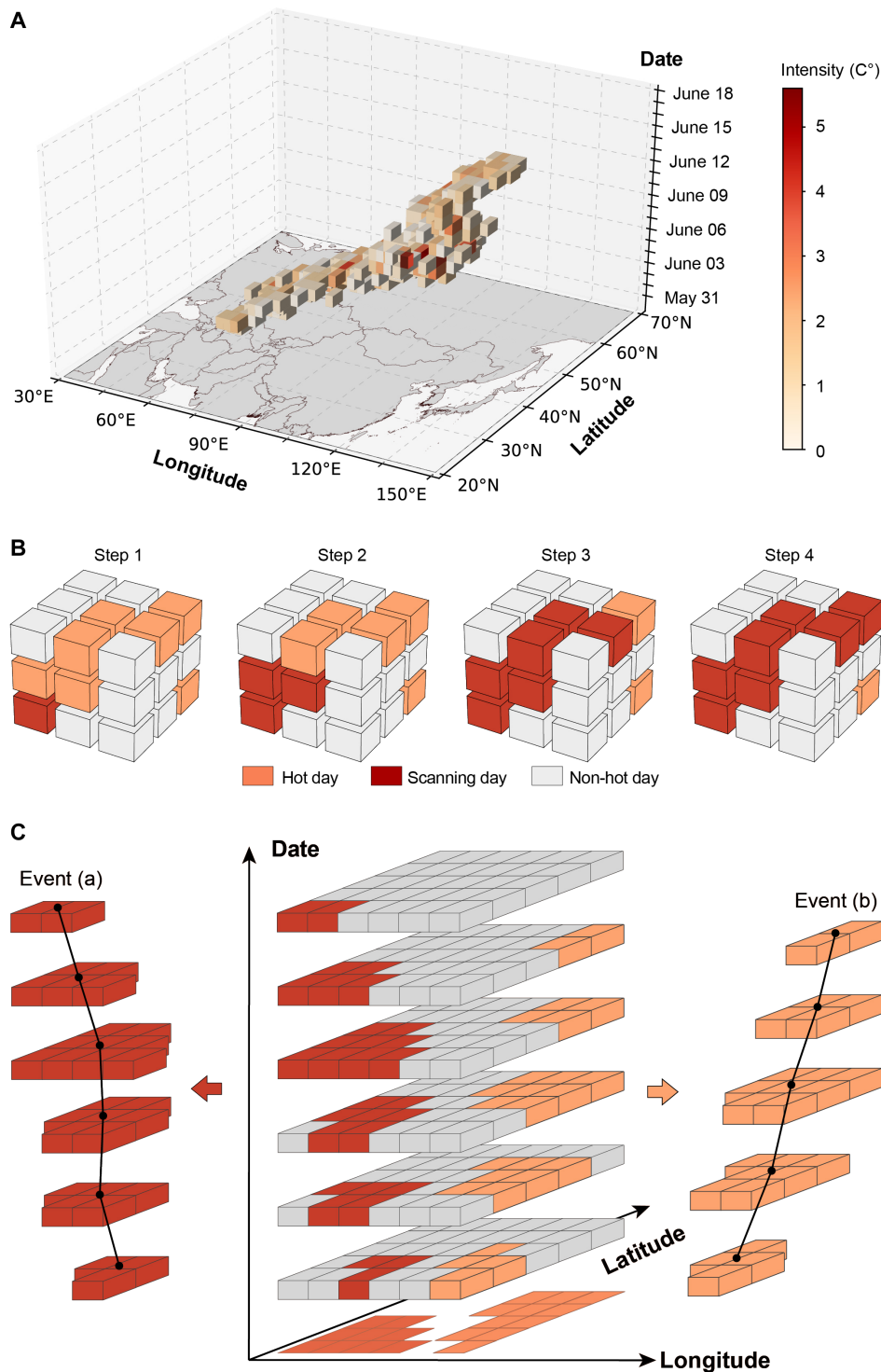


Fig. 1. Identification of spatiotemporally contiguous heatwave event based on 3D 26-connectivity tracking. (A) Spatiotemporal evolution of a contiguous heatwave event from 31 May to 17 June 1997. (B) Scanning process of tracking contiguous heatwaves that are spatiotemporally connected by the 3D-connected component (CC3D)-labeling algorithm with the connectivity of 26 along three dimensions of latitude \times longitude \times time, with gray grid indicating the non-hot day, the orange grid indicating the hot day, and the red grid denoting the scanning day. (C) Diagram of identifying spatiotemporally contiguous heatwave events. The red and orange colors show the two contiguous heatwave events that move toward different directions, with the black dots denoting the geographical centroids of each day of the event.

Table 1. Summary of the metrics used in this study to characterize spatiotemporally contiguous heatwaves.

| Metric | Description |
|---------------------------------------------------------------|------------------------------------------------------------------------------------------------------------------------------|
| Frequency (event) | Total amount of the corresponding contiguous heatwave events that occur in the summertime within a year |
| Total magnitude ($10^6 \text{ km}^2 \times ^\circ\text{C}$) | Area-aggregated sum of the temperature exceedance relative to the threshold over all grid cells across all days of the event |
| Intensity ($^\circ\text{C}$) | Area-weighted average of the maximum temperature exceedance over all grid cells across all days of the event |
| Accumulated area (10^6 km^2) | Sum of the areal extent of all grid cells across all days of the event |
| Lifetime (days) | Time interval between the beginning and end of the event (the height of the contiguous heatwave structure) |
| Mean duration (days) | Mean value of the durations of all grid cells associated with the event |
| Total moving distance (10^3 km) | Sum of the centroid moving distance between adjacent time steps over the whole lifespan of the event |
| Moving speed (km/day) | Ratio of the total moving distance of the event to the lifetime of the event |
| Moving direction | Directional angle from the centroid location of the first half of the event to the second centroid location of the event |

heatwaves is shown in Fig. 2A, with the size and color of the circle respectively representing the accumulated area and intensity of contiguous heatwaves based on daily maximum temperature of the ERA5 reanalysis dataset. As shown in Fig. 2A and figs. S1A and S2A, three different datasets (ERA5, MERRA2, and NCEP2) yield similar spatial distributions of contiguous heatwaves, with the average accumulated area being about 7 million km^2 (6.48×10^6 , 6.47×10^6 , and $5.94 \times 10^6 \text{ km}^2$ for ERA5, MERRA2 and, NCEP2, respectively). Consistent results are also seen in different temperature indicators including daily minimum temperature (T_{\min}) and wet bulb temperature (T_w) (figs. S3A and S4A).

The accumulated area exhibits remarkable regional differences in relation to the latitude and the distribution of the global land surfaces. It is found that the accumulated area decreases as the latitude increases in the mid- and high-latitude regions, and it increases as the latitude increases in the low-latitude regions. The accumulated area of heatwaves is smaller in the low latitudes ($5.84 \times 10^6 \text{ km}^2$) and larger in the mid- and high-latitudes ($7.13 \times 10^6 \text{ km}^2$). In contrast, the intensity of contiguous heatwaves (see Materials and Methods and Table 1) increases with the latitude in the low- and midlatitude regions, reaching its maximum around 50°N to 60°N (50°S to 60°S) in the Northern (Southern) Hemisphere. The relationship between the intensity and latitude coincides with stronger temperature variability in higher than lower latitudes (21). To further investigate the regional characteristics of the contiguous heatwaves, we first rank the contiguous heatwaves by the accumulated area in each continent and then select the top 40% of events in each continent for further regional analyses. The mean values of multidimensional heatwave metrics in different continents, as selected by relative thresholds are summarized in tables S1 to S3. On the basis of the latitude of the centroid for heatwaves, we find that the events in the Northern Hemisphere (1522 events) with a mean latitude of 52.52°N tend to have larger accumulated areas ($7.75 \times 10^6 \text{ km}^2$) than the events (1021 events) with a mean latitude of 19.99°S in the Southern Hemisphere ($5.08 \times 10^6 \text{ km}^2$) (table S1).

Figure 2B presents the lifetime and moving patterns (including moving direction and distance; see also Table 1 for details) of the

centroids of contiguous heatwaves from 1979 to 2020. Most of the contiguous heatwaves (60.28%) prefer to move from west to east (Fig. 2B). In the Northern Hemisphere, the heatwaves in the mid- to high-latitudes and inland areas tend to develop from west to east (fig. S5), likely modulated by the eastward movement of the Rossby waves and the associated atmospheric blocking (22), which suppress the intrusion of cold air and favor the maintenance of the anomalously high-pressure system (23). While the events in lower latitudes and coastal areas are often originated from the east or the adjacent oceans (fig. S5). For example, the development of heatwaves in the coastal southern China are triggered by a westward extension of the western North Pacific subtropical high (24). Moreover, we also conduct an additional experiment by including the ocean regions surrounding the continents by applying a buffering zone of 250 km to the enveloped extent of the global land areas, which ensures that at least one grid point in the ocean surrounding the continents can be included. In this sense, any heatwaves moving from or toward the ocean can be tracked and analyzed. The moving pattern of the large contiguous heatwaves over the land area and the surrounding oceans within a buffer zone of 250 km are shown in fig. S6A. As it indicates, these events also mainly tend to move from west to east, and their patterns are highly consistent with our previous results, further demonstrating the robustness of our analyses.

The regional discrepancies in the moving patterns of large contiguous heatwaves in different continents are noticeable (Fig. 2C). The events in Eurasia and North America have longer durations and shorter distance, with an average lifetime (moving distance) of 10.20 days (340.23 km) and 9.69 days (296.93 km), respectively (Fig. 2B and table S1). These events are closely linked to the atmospheric blocking and local processes (i.e., land-atmosphere feedbacks). On the one hand, long-lived blocking favors the persistent high-pressure system and is thus conducive to the longer-lasting heatwaves (25). On the other hand, persistent warming during heatwaves can dry soil by increasing evaporative demand, which in turn transmits incoming radiant energy to the atmosphere and warms the near-surface air via increased sensible heat flux (26, 27). This feedback can thereby prolong the life expectancy of the heatwave event (27). Long-lived heatwaves may cause more

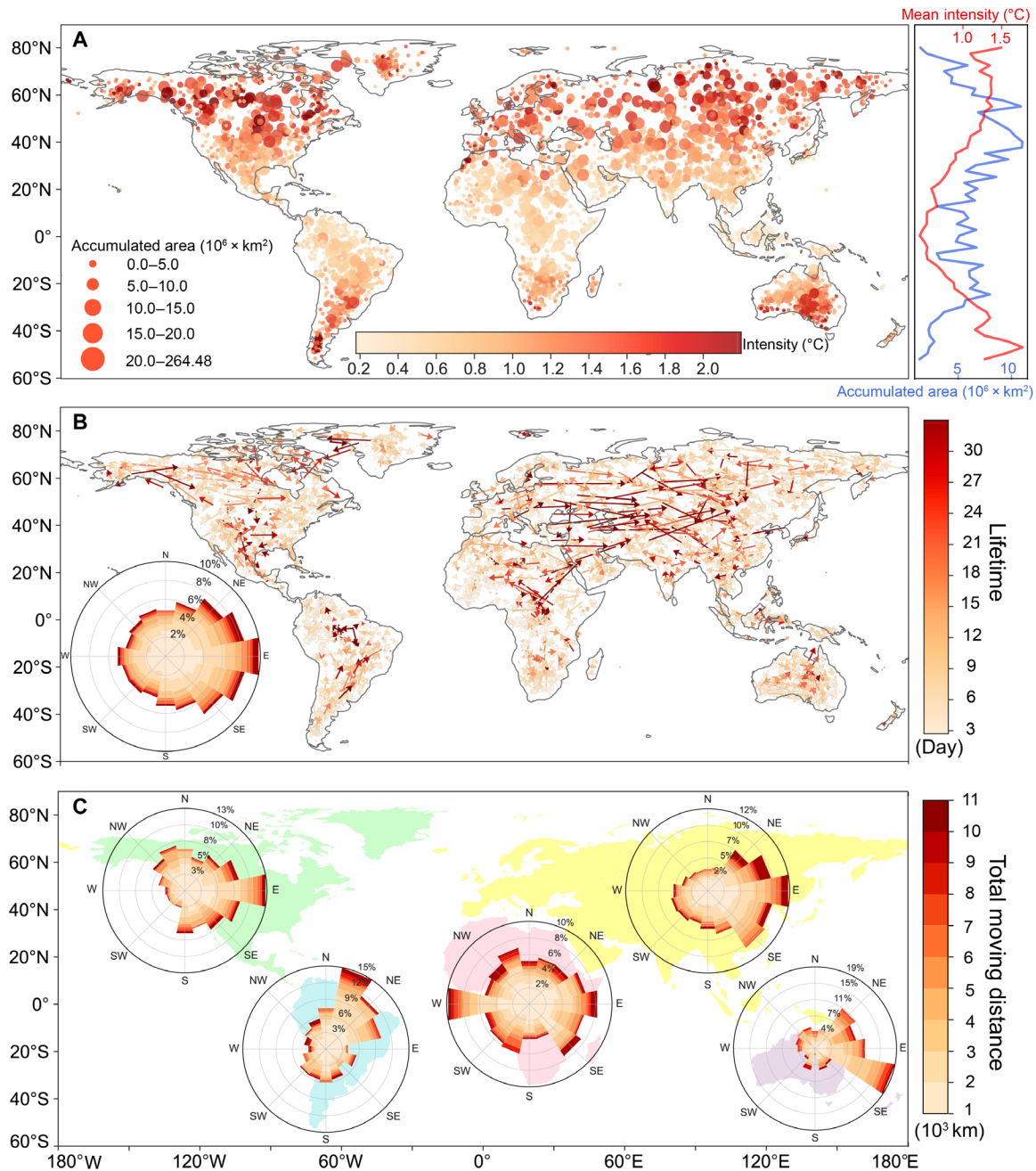


Fig. 2. Spatial distribution of the contiguous heatwaves from 1979 to 2020. (A) Distribution of the centroids of the entire contiguous heatwaves, with the size and color denoting their accumulated area and intensity, respectively. Right, shows the changes in the accumulated area (i.e., denoted by the blue line) and intensity (i.e., denoted by the red line) with latitude. (B) Distribution of the movement of the contiguous heatwaves, with the color denoting the lifetime of the contiguous heatwaves. The embedded rose diagram shows the directional distribution of the moving distance of the contiguous heatwaves, with the percentage value indicating the proportion of moving distance along a certain direction. (C) Contiguous heatwaves are selected from the top 40% of events in each continent. Each rose diagram shows the directional distribution of the movement of the contiguous heatwaves in different continents, with the color indicating the shift distance from the centroid of the first half of the event to the centroid of the second half, and the percentage value representing the proportion of moving distance along a certain direction.

persisting damages, thus leading to more adverse impacts on these regions. Most of the contiguous heatwaves in Eurasia (62.84%) and North America (62.35%) move from west to east during their lifetime, and nearly half of the events (52.65%) in North America exhibit northward propagation (Fig. 2C). The eastward-moving tendencies can also be found in Australia, where the southeastward propagation prevails

(Fig. 2C). The predominant southeastward-moving heatwaves in Australia are possibly linked to a slow-moving transient anticyclone, which is accompanied by northwesterly flow over the southeast of Australia (28, 29). For contiguous heatwaves in South America, their northeastward movements are likely associated with the jet stream that transports warm air from the inland regions toward the coasts and further

northeastward (30). In contrast to the aforementioned continents, Africa witnesses the nearly same number of eastward (51.16%) and westward (48.84%) contiguous heatwaves (Fig. 2C). The moving directions of heatwaves over Africa are more scattered, which may suggest that those heatwaves are less influenced by Rossby waves and midlatitude weather patterns in the tropics (31, 32). The other two reanalysis datasets (MERRA2 and NCEP2) yield similar results of contiguous heatwaves across the globe and continents in terms of spatial distribution and propagation (figs. S1 and S2). In addition, the directional distribution of the movement of contiguous heatwaves derived from the extended global land including the ocean regions surrounding the continents is provided in fig. S6. As it shows, the Eurasian and North American heatwaves also mainly move eastward, and South American heatwaves tend to move northeastward. These results are consistent with those in Fig. 2, demonstrating that considering ocean regions surrounding the continents does not affect the heatwave tracking in the inland regions and the moving direction of the tracked heatwaves as well.

Temporal changes of contiguous heatwaves from 1979 to 2020

In addition to spatial distribution and propagation, contiguous heatwaves also exhibit remarkable temporal changes. We now assess long-term temporal changes in the warm-season contiguous heatwaves since 1979, in terms of frequency, magnitude, areal extent, duration, and moving properties (Fig. 3, A to C, and fig. S7). All heatwave metrics except for moving speed and average intensity show significant increasing trends (P value < 0.05). From 1979 to 2020, the annual mean frequency of these events is at an increasing rate of 8.33 events per decade, which increases from 75.2 events averaged over the first 5-year period from 1979 to 1983 to 98.2 events over the past

5-year period from 2016 to 2020 (Fig. 3A). The accumulated area ($9.52 \times 10^5 \text{ km}^2$ per decade; fig. S7A) and total magnitude ($9.91 \times 10^5 \text{ km} \times ^\circ\text{C}$ per decade; fig. S7D) also exhibit significant increases (P value < 0.05). The annual maximum heatwave intensity, as measured by the maximum temperature exceedance, shows a significant increasing trend of 0.09°C per decade (P value < 0.05 ; fig. S7E). However, the annual average intensity exhibits a weak decrease of -0.02°C per decade (fig. S7F). This decrease mainly arises from the decreasing intensity of tropical heatwaves that also have a greater increase in the frequency, while those in higher latitudes exhibit an increasing intensity trend and a smaller increase in the frequency (fig. S8). The changes in the average intensity are consistent with Perkins-Kirkpatrick and Lewis (33) and Rogers *et al.* (19), who found unchanged average heatwave intensity and even decreases in some parts of the globe, as well as the global average.

The lifetime (1.02 days per decade, P value < 0.05) and mean duration (0.30 days per decade, P value < 0.05) of these events significant increase (fig. S7, B and C), from 8.17 days (2.23 days) averaged over the first 5-year period to 12.15 days (3.49 days) over the past 5-year period, which are particularly over Eurasia with a markedly higher rate (1.15 and 0.25 days per decade for lifetime and mean duration, respectively) than in other continents (fig. S9). Significant increasing trends are also found in the total moving distance (285.19 km per decade, P value < 0.05 ; Fig. 3B), from $2.43 \times 10^3 \text{ km}$ averaged from 1979 to 1983 to $3.40 \times 10^3 \text{ km}$ from 2016 to 2020. The largest increments in total moving distance appear in South America ($0.53 \times 10^3 \text{ km}$ per decade; fig. S9), and the smallest ones appear in Australia ($0.17 \times 10^3 \text{ km}$ per decade; fig. S9). In addition, there is a significant global slowdown in moving speed, at a rate of -9.19 km/day per decade (P value < 0.05 ; Fig. 3C). These results suggest that

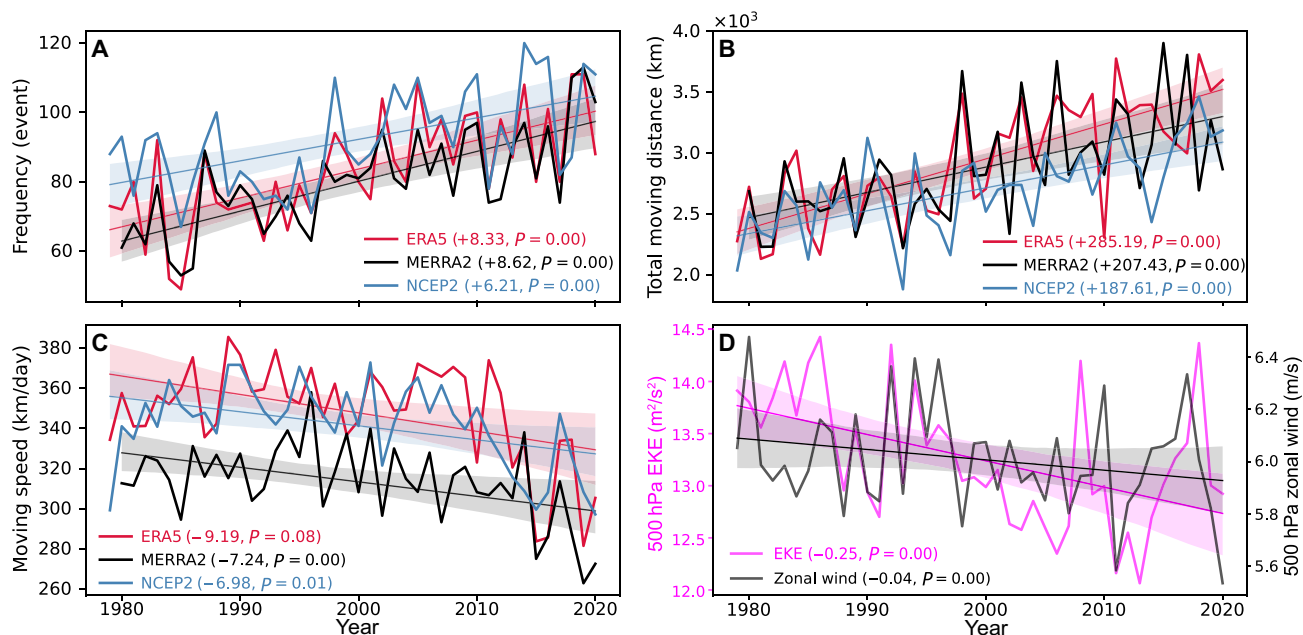


Fig. 3. Observed temporal changes of the warm-season contiguous heatwaves from 1979 to 2020. (A) Frequency of the contiguous heatwaves based on three reanalysis datasets: ERA5, MERRA2, and NCEP2. (B) and (C) are the same as (A) but for the total moving distance and moving speed of the contiguous heatwaves, respectively. (D) Temporal changes in summer 500 hPa EKE and U over the land areas of the Northern Hemisphere from 1979 to 2020. The solid curve denotes the values of temporal changes. The straight line indicates the corresponding linear trend. The shading indicates the 95% confidence interval of the fitted line. Slope and P values estimates for the trend per decade are given in parentheses.

contiguous heatwaves occur more frequently, cover larger areas, persist longer, travel longer, and move slower. We also examine the temporal changes in multiple heatwave metrics over the full calendar year, and these results (see fig. S10) agree well with those based on seasonal heatwaves, demonstrating the robustness of our investigation. These changes have also been detected in other datasets (MERRA2 and NCEP2; see Fig. 3, A to C, and figs. S7 and S9) and other temperature indicators (T_{\min} and T_w ; see figs. S11 and S12).

To attribute the above long-term changes, we examine large contiguous heatwaves simulated by Coupled Model Intercomparison Project Phase 6 (CMIP6) models (Fig. 4, A to C; see Materials and Methods for details). There are upward trends in the frequency and total travel distance, and a downward trend in the moving speed from 1979 to 2020, which can be replicated by the experiments with natural and anthropogenic forcings (hist-ALL). The increasing trends in the frequency cannot be captured by the experiments with natural-only forcing (hist-NAT), while the trends in the moving distance (42.86 km per decade, P value < 0.05) and moving speed (-4.18 km/day per decade, P value < 0.05) are significant for hist-NAT. The trends of moving speed in hist-NAT experiments (-4.18 km/day per decade) are much weaker than those in hist-ALL (-9.81 km/day per decade) and greenhouse gas forcing (hist-GHG) (-8.43 km/day per decade) experiments. Meanwhile, the trends of moving speed are likely related to the Atlantic Multidecadal Oscillation (AMO) (see fig. S13), as negative to positive AMO phase shift in recent decades can change the midlatitude jet stream causing persistent heatwaves and weaken the zonal wind (U), thus slowing down the heatwave propagation (34, 35). Quantitatively, the increasing trend in the frequency (8.96 events per decade) and moving distance (213.51 km per decade), and the decreasing trend in the moving speed (-8.43 km/day per decade) from

the hist-GHG simulation are similar to those of the hist-ALL simulation (7.85 events per decade, 236.96 km per decade, and -9.81 km/day per decade), suggesting the dominant role of GHG. While the slowdown in the moving speed of heatwaves is jointly influenced by anthropogenic forcing, natural forcing, and natural climate variability, anthropogenic forcing is the main driver responsible for more frequent, longer-lived, and slower-moving large contiguous heatwaves.

Considering that contiguous heatwaves in the Northern Hemisphere have relatively longer moving distances (partially linked to a larger amount of northern land areas) and slower moving speed than the Southern Hemisphere (table S1), the temporal changes (fig. S14) and possible mechanisms (Figs. 3D and 4D) in the Northern Hemisphere are examined. Previous studies have shown that midlatitude circulation changes are closely associated with changes of extreme weather and climate events in boreal summer (36, 37). Therefore, EKE and U at the 500 hPa level are calculated to understand the dynamic evolution properties including the moving distance and speed of contiguous heatwaves (Figs. 3D and 4D). The 1979-to-2020 period has seen a significant long-term decline in summertime EKE (-0.25 $\text{m}^2 \text{s}^{-2}$ per decade, P value < 0.05), and this decline is accompanied by a decrease in the zonal-mean U (-0.04 m/s per decade, P value < 0.05), which indicates a weakening of the zonal jet stream and possible reduction in the amplitudes of fast-moving synoptic wave activity (36). These changes signify an increased frequency of persistent circulation patterns that produce and maintain more persistent weather conditions (36, 38, 39), thus may intensify contiguous heatwaves by increasing the accumulated area, duration, and moving distance. To test this hypothesis, we calculate the Pearson's correlation coefficients between the time series of EKE and U with the moving distance and speed of

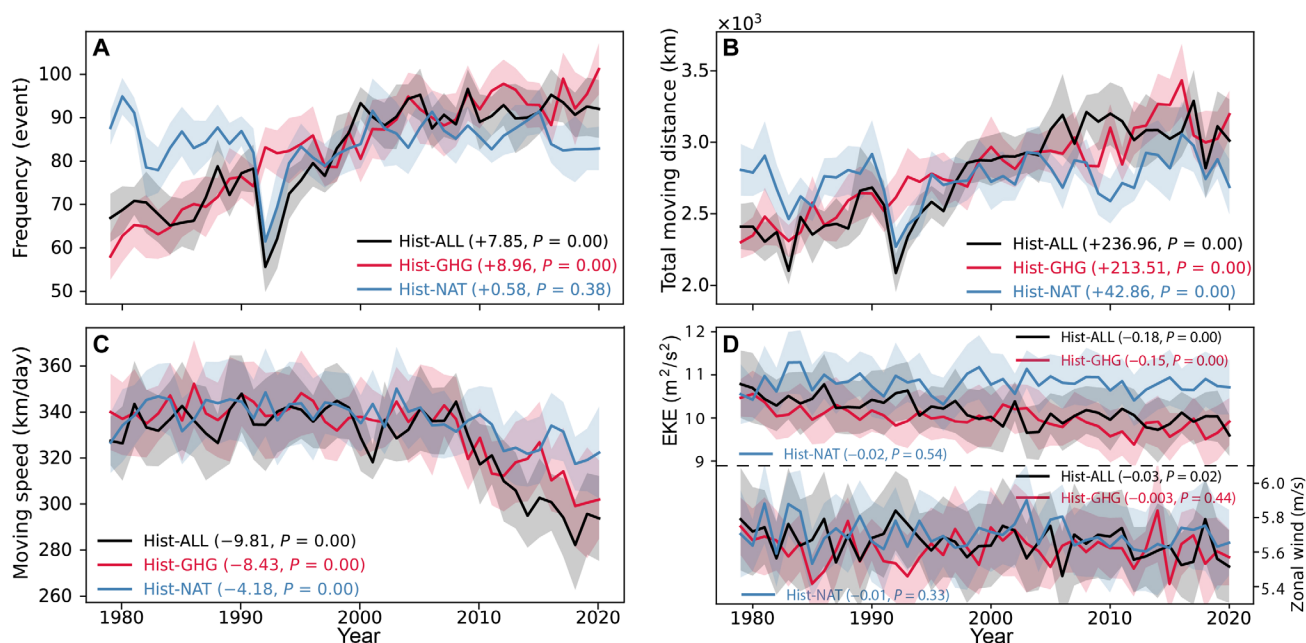


Fig. 4. Simulated temporal changes of the warm-season contiguous heatwaves from 1979 to 2020. (A) Frequency of the contiguous heatwaves in CMIP6 simulations under hist-GHG, hist-ALL, and hist-NAT forcings. (B) and (C) are the same as (A) but for the total moving distance and moving speed of the contiguous heatwaves, respectively. (D) Temporal changes in summer 500 hPa EKE and U over the land areas of the Northern Hemisphere from 1979 to 2020. The solid curve denotes the values of temporal changes. The shading indicates the corresponding intermodel spread estimated by the SD among all available CMIP6 models. Slope and P values estimates for the trend per decade are given in parentheses.

contiguous heatwaves in the land areas of the Northern Hemisphere. EKE associated with synoptic-scale weather systems has a significant correlation with the abovementioned heatwave metrics, with values of -0.44 (P value < 0.05) and 0.28 (P value < 0.1) for the moving distance and speed, respectively. Significant correlation coefficient is also identified between 500-hPa U and the moving distance of contiguous heatwaves, with a value of -0.46 (P value < 0.05). The declining EKE and U are well produced in the hist-ALL and hist-GHG runs of CMIP6 simulations (table S4), demonstrating the impact of anthropogenic GHG emissions on decreasing EKE and U, especially in the Northern Hemisphere. The slowing transient waves can provide more favorable and persistent conditions for maintaining heat extremes over the continents.

To further examine the role of the EKE variability in the moving speed, linear regression analyses are applied at each grid point between the detrended EKE anomalies and the detrended geopotential height anomalies at 500 hPa over the Northern Hemisphere in the summer season (fig. S15A). We find that widespread and significant negative correlations (P values < 0.05) between EKE and geopotential height anomalies are seen over the Northern Hemisphere. This result indicates that lower EKE is associated with positive geopotential height anomalies (i.e., high-pressure systems), thus creating favorable conditions for atmospheric blocking and persistent weather conditions over these regions in summer (40). These changes are conducive to reducing the moving speed of the heatwaves. Notably, significant decreasing trends (P values < 0.05) in summer EKE are observed over the eastern North America and most regions of Eurasia (fig. S15B). As reported by Horton *et al.* (41), these regions also show upward trends in the frequency and persistence of summertime anticyclonic circulation patterns since 1979, contributing to more and longer high-temperature extremes. Moreover, the decline in EKE is associated with a reduction in the zonal flow (36), thus further decreasing the moving speed of the heatwave.

Temporal changes of contiguous heatwaves in more recent decades

It is also observed in fig. S16 that the trend since the late 1990s is stronger than that from 1979 to the mid-1990s. The trends in the accumulated area, lifetime, total magnitude, and total moving distance continue to increase in magnitude and remain significant from 1979–1996 to 1997–2020. For example, the accumulated area and moving distance of contiguous heatwaves increase by over 0.33×10^6 km² and 0.10×10^3 km per decade from 1979 to 1996, and these trends have accelerated to 0.88×10^6 and 0.20×10^3 km per decade from 1997 to 2020. The changing rate of the heatwave lifetime increases from 0.13 days per decade from 1979 to 1996 to 1.47 days per decade from 1997 to 2020. The increasing trend in the frequency (1.32 events per decade, P value = 0.82) and mean duration (-0.02 days per decade, P value = 0.21) are slight and not significant from 1979 to 1996, while they have accelerated to 5.31 events per decade and 0.62 days per decade from 1997 (P value < 0.05), respectively. This means that the contiguous heatwaves are becoming more frequent, covering larger areas and traveling longer. The acceleration of the observed trends of heatwave frequency, area, duration, and moving distance is expected in view of global warming and its associated midlatitude circulation changes (33, 42, 43).

The moving speed of large contiguous heatwaves has significantly slowed since the 1990s (fig. S16I), at a rate of -24.87 km/day per decade (P value < 0.05), which is stronger than the rate before the

1990s (13.76 km/day per decade). As shown in table S5, this slowdown is especially prominent in Africa (-30.24 km/day per decade with P value < 0.1) and Eurasia (-23.61 km/day per decade with P value < 0.05). Compared with the ERA5 dataset, this significant slowdown of the moving speed is also seen in the other datasets, with values of -16.44 and -20.21 km/day per decade with P value < 0.05 at a global scale for MERRA2 and NCEP2, respectively (fig. S17I and S18I and tables S6 and S7). We find a shift toward slower speed in recent decades, suggesting that slowing movement of heatwaves would have more persistent and profound effects on local societies, as the locally accumulated damages by heatwaves can substantially intensify under slow movements. This slowdown may elevate the risks of ecosystem productivity reduction and increase the consumptions and capacity needs in energy sectors (fig. S19).

In summary, this study has provided global assessment of the changes in moving patterns of contiguous heatwaves. Our findings suggest that the characteristics of contiguous heatwaves are heterogeneous across different continents with increases in the frequency, duration, magnitude, areal extent, and moving distance in large terrestrial contiguous heatwaves since 1979. The significant decreasing trends of moving speed and the increasing trends of the frequency and traveling distance are likely caused by anthropogenic forcing over the past decades. Our results are robust among different datasets and different temperature indicators. Beyond previous studies of the heatwaves based on fixed stations or grid cells, our global assessment from the evolution perspective has provided a more comprehensive picture of how heatwave events jointly evolve in both space and time. Moreover, we have improved the understanding of the characteristics of the slower and hotter contiguous heatwaves. The results suggest that longer-traveling and slower-moving large contiguous heatwaves will cause more devastating impacts on natural and societal systems in the future if GHG keep rising, and no effective mitigation measures are taken.

MATERIALS AND METHODS

Observational and model data

We use daily maximum temperature at 2-m height (T_{\max}) over the period from 1979 to 2020 from the recently released ERA5 reanalysis dataset (44) to track spatiotemporally contiguous heatwaves. Daily T_{\max} was calculated from the hourly near-surface air temperature at 2-m height. Produced by the European Centre for Medium-range Weather Forecasts, the ERA5 global reanalysis is a fifth-generation product that replaces ERA-Interim and improves on other surface weather reanalysis with respect to temperature, precipitation, and wind speed (44). We also compare the results based on ERA5 with other reanalysis products including the NCEP-DOE Reanalysis 2 [NCEP2, (45)] from 1979 to 2020 and the Modern-Era Retrospective analysis for Research and Applications, version 2 [MERRA2, (46)] from 1980 to 2020. The temperature metrics used for NCEP2 and MERRA2 are both the daily maximum temperatures at 2-m height above the ground. The original horizontal resolution of ERA5, MERRA2, and NCEP2 are $0.25^\circ \times 0.25^\circ$, $0.5^\circ \times 0.625^\circ$, and $1.90^\circ \times 1.875^\circ$, respectively, and all three reanalysis products are regridded into the resolution of $2.5^\circ \times 2.5^\circ$ by the bilinear interpolation for comparison. Both NCEP2 and MERRA2 yield consistent results with ERA5 in terms of similar spatial distributions and temporal changes in the contiguous heatwaves (see the Supplementary Materials), demonstrating the robustness of our investigation. We also use the daily

minimum temperature (T_{\min}) and wet bulb temperature [T_w , (47)] to derive nighttime and humid heatwaves, respectively. The results of T_{\min} and T_w are consistent with those of T_{\max} (see the Supplementary Materials).

To assess the extent to which external forcing influences the observed changes in historical heatwave metrics, we use daily T_{\max} outputs from 11 global climate models participating in the CMIP6 (see table S8 for details), including historical simulations forced by hist-NAT, anthropogenic hist-GHG, and historical forcing (hist-ALL, including all natural and anthropogenic forcings). To keep the consistency with the observational datasets, the CMIP6 outputs are interpolated onto a horizontal resolution of $2.5^\circ \times 2.5^\circ$ by the bilinear interpolation. For each forcing, we first derive the heatwave metrics from each model simulation separately and then average the metrics of all participating model simulations to obtain the multi-model mean (i.e., ensemble mean). The ensemble mean is used to remove the uncertainties from model differences. Except for hist-ALL ending in 2014, both hist-NAT and hist-GHG runs end in 2020. Previous studies often used the shared socioeconomic pathways (SSP) 2-4.5 to extend hist-ALL simulations, as the SSP2-4.5 pathway can match the current economic development path best (48–50). We combine the simulation from SSP2-4.5 to extend the hist-ALL simulations to 2020. To evaluate the robustness of this extension, we also use the SSP1-2.6, SSP3-7.0, and SSP5-8.5 scenarios to extend the hist-ALL simulations (fig. S20) and find that the trends based on extended hist-ALL simulations by SSP2-4.5 are consistent with other SSP scenarios (table S9).

Tracking of contiguous heatwaves

In this study, the contiguous heatwaves are defined as the events with extreme high temperatures (exceeding the 95th percentile) that persist for a total period of time (≥ 3 days) and cover a certain areal extent (≥ 1 grids) in three dimensions of latitude \times longitude \times time, similar to previous regional studies (15, 20). A fast-moving contiguous heatwave event may affect certain grid cells for 1 or 2 day(s). In particular, we track the three-dimensional (3D) contiguous heatwaves from the gridded daily T_{\max} values that are stored in a 3D array with three dimensions using a spatiotemporally contiguous events tracking (SCET) method based on the 3D-connected component (CC3D) labeling algorithm as implemented in the Python package connected-components-3d (<https://pypi.org/project/connected-components-3d/>) (51). A grid cell (i.e., a grid point with three dimensions of latitude \times longitude \times time) of the 3D array is first marked as “1” if daily T_{\max} at the grid point exceeds the 95th percentile of T_{\max} on the same calendar day centered on a 15-day window in 1981 to 2010 (a set of $15 \times 30 = 450$ days) and as “0” if the 95th percentile is not exceeded. Using this screening, the 3D array of T_{\max} values is then converted into a 0/1 binary format and inputted into the CC3D algorithm. All 1s that are adjacent in 26 neighbors are connected as an individual contiguous heatwave event (51). The 26-connectivity considers all the surrounding neighbors (nine on the previous day, eight on the current day by excluding the center grid, and nine on the next day) by both adjacent and diagonal connectivity, and it allows tracking the contiguous heatwave events simultaneously in both space and time (see Fig. 1B). The 26-connectivity searching allows a contiguous event to break into parts and connect again, providing that they are contiguous either in space or in time. In addition, this tracking algorithm can also ensure that individual contiguous heatwaves are neither spatially nor temporally adjacent (Fig. 1C). We

also examine the merging events that may have been separated by 1 day or one grid cell and find that the results are consistent (fig. S21).

This tracking identifies extreme events in all seasons of the calendar year, and we focus on examining the events in the hot summer season only, which is defined as June–July–August (JJA) for the Northern Hemisphere and December–January–February (DJF) for the Southern Hemisphere (52, 53). The heatwaves in the summer seasons are selected on the basis of the location of the centroid of the events. If the centroid of an event is located in the Northern Hemisphere and occurs in the JJA season, then it is selected as a Northern Hemisphere heatwave; if the centroid of an event is located in the Southern Hemisphere and occurs in DJF, then it is selected as a Southern Hemisphere heatwave. Considering that large contiguous heatwaves often cause more prominently adverse societal impacts, we select the large contiguous heatwaves with the accumulated area ≥ 1 million km^2 and assess their evolution and moving patterns in the globe. To make the results between the different continents comparable, we set different heatwave sizes for different continents. For each continent, we first rank the heatwave events by the accumulated area and then select the top 40% of events for further analyses.

Metrics of contiguous heatwaves

Contiguous heatwave events are characterized by multidimensional metrics, including frequency, magnitude, intensity, duration, areal extent, and evolution patterns (including moving distance, moving speed, and moving direction; see Table 1 for details). Here, total magnitude refers to the accumulated temperature exceedance relative to the extreme threshold multiplied by the area of all grid points associated with the event, that is, the sum of the product of the exceedance and the area of the corresponding day, thus having a unit of $10^6 \text{ km}^2 \times ^\circ\text{C}$, while intensity (unit: $^\circ\text{C}$) refers to maximum temperature exceedance by weighting the area of grid point. The accumulated area is defined as the sum of the areal extent of all grid cells across all days of the event. Similarly, the lifetime is computed as time interval between the beginning and end of the event. The evolution pattern including total moving distance, moving direction, and moving speed is determined by the centroids of the contiguous heatwave event. The centroid is calculated as the mean geographical location (latitude and longitude) of all grid cells over the participating days of the event by weighting the area and the temperature exceedance relative to the threshold (95th percentile) (20). Thus, the moving directions are calculated as the angle between the centroid of the first half event and the centroid of the second half event. Details on the definition of these metrics are summarized in Table 1.

The yearly series of multidimensional metrics of these large contiguous heatwaves are calculated by averaging all events occurring in the summer of the corresponding year. Simple linear regression is used to calculate the long-term trends in the yearly series, and their statistical significance is estimated by the nonparametric modified Mann-Kendall trend test (54).

Derivation of EKE

Large-scale midlatitude atmosphere processes can be characterized by fast-traveling Rossby wave associated with cyclones (low-pressure systems) and anticyclones (high-pressure systems) (36, 55). These fast-traveling Rossby waves (with zonal wave numbers about six to eight) mostly occur as high-amplitude and synoptic transients (36, 56), which arise from a variety of energy sources (e.g., the eddy-driven phenomena) (36, 55, 57) and can trigger the weather variability at

synoptic scales (58). Referring to Boer and Shepherd (57), the interaction between intensity and frequency of these transient waves can be measured by the total EKE, which is approximately equally partitioned between the zonal (u) and meridional wind (v) components (59): $E'_k = \frac{1}{2}(u'^2 + v'^2)$, where u' and v' are synoptic scale (2 to 8 days) zonal and meridional wind components, respectively (36, 59). In this study, we apply a 2- to 8-day band-pass filter to extract EKE at the synoptic scale over the land areas of the Northern Hemisphere [30°N to 90°N, following Coumou *et al.* (36)].

Supplementary Materials

This PDF file includes:

Figs. S1 to S21

Tables S1 to S9

References

REFERENCES AND NOTES

- J. Yang, M. Zhou, Z. Ren, M. Li, B. Wang, D. L. Liu, C.-Q. Ou, P. Yin, J. Sun, S. Tong, H. Wang, C. Zhang, J. Wang, Y. Guo, Q. Liu, Projecting heat-related excess mortality under climate change scenarios in China. *Nat. Commun.* **12**, 1039 (2021).
- Y. Zhao, B. Sultan, R. Vautard, P. Braconnot, H. J. Wang, A. Ducharne, Potential escalation of heat-related working costs with climate and socioeconomic changes in China. *Proc. Natl. Acad. Sci. U.S.A.* **113**, 4640–4645 (2016).
- D. García-León, A. Casanueva, G. Standardi, A. Burgstall, A. D. Flouris, L. Nybo, Current and projected regional economic impacts of heatwaves in Europe. *Nat. Commun.* **12**, 5807 (2021).
- S. Kang, E. A. B. Eltahir, North China plain threatened by deadly heatwaves due to climate change and irrigation. *Nat. Commun.* **9**, 2894 (2018).
- K. K. Zander, W. J. W. Botzen, E. Oppermann, T. Kjellstrom, S. T. Garnett, Heat stress causes substantial labour productivity loss in Australia. *Nat. Clim. Change* **5**, 647–651 (2015).
- J. E. Hopke, Connecting extreme heat events to climate change: Media coverage of heat waves and wildfires. *Environ. Commun.* **14**, 492–508 (2019).
- Y. Qian, P.-C. Hsu, J. Yuan, Z. Zhu, H. Wang, M. Duan, Effects of subseasonal variation in the east asian monsoon system on the summertime heat wave in western north America in 2021. *Geophys. Res. Lett.* **49**, e2021GL097659 (2022).
- J.-M. Robine, S. L. K. Cheung, S. Le Roy, H. Van Oyen, C. Griffiths, J.-P. Michel, F. R. Herrmann, Death toll exceeded 70,000 in Europe during the summer of 2003. *C. R. Biol.* **331**, 171–178 (2008).
- M. M. Vogel, J. Zscheischler, E. M. Fischer, S. I. Seneviratne, Development of future heatwaves for different hazard thresholds. *J. Geophys. Res. Atmos.* **125**, e2019JD032070 (2020).
- G. A. Meehl, C. Tebaldi, More intense, more frequent, and longer lasting heat waves in the 21st century. *Science* **305**, 994–997 (2004).
- IPCC, *Climate Change 2021: The Physical Science Basis. Contribution of Working Group I to the Sixth Assessment Report of the Intergovernmental Panel on Climate Change* (Cambridge Univ. Press, 2021).
- S. E. Perkins, L. V. Alexander, J. R. Nairn, Increasing frequency, intensity and duration of observed global heatwaves and warm spells. *Geophys. Res. Lett.* **39**, L20714 (2012).
- B. Lyon, A. G. Barnston, E. Coffel, R. M. Horton, Projected increase in the spatial extent of contiguous US summer heat waves and associated attributes. *Environ. Res. Lett.* **14**, 114029 (2019).
- D. Keellings, H. Moradkhani, Spatiotemporal evolution of heat wave severity and coverage across the United States. *Geophys. Res. Lett.* **47**, e2020GL087097 (2020).
- P. J. Reddy, S. E. Perkins-Kirkpatrick, J. J. Sharples, Interactive influence of ENSO and IOD on contiguous heatwaves in Australia. *Environ. Res. Lett.* **17**, 014004 (2021).
- S. E. Perkins, L. V. Alexander, On the measurement of heat waves. *J. Climate* **26**, 4500–4517 (2013).
- Q. You, Z. Jiang, L. Kong, Z. Wu, Y. Bao, S. Kang, N. Pepin, A comparison of heat wave climatologies and trends in China based on multiple definitions. *Climate Dynam.* **48**, 3975–3989 (2017).
- D. Keellings, E. Bunting, J. Engström, Spatiotemporal changes in the size and shape of heat waves over North America. *Clim. Change* **147**, 165–178 (2018).
- C. D. W. Rogers, K. Kornhuber, S. E. Perkins-Kirkpatrick, P. C. Loikith, D. Singh, Sixfold increase in historical Northern Hemisphere concurrent large heatwaves driven by warming and changing atmospheric circulations. *J. Climate* **35**, 1063–1078 (2022).
- M. Luo, G. Lau, Z. Liu, S. Wu, X. Wang, An observational investigation of spatiotemporally contiguous heatwaves in China from a 3D perspective. *Geophys. Res. Lett.* **49**, e2022GL097714 (2022).
- T. Tamarin-Brodsky, K. Hodges, B. J. Hoskins, T. G. Shepherd, A dynamical perspective on atmospheric temperature variability and its response to climate change. *J. Climate* **32**, 1707–1724 (2019).
- S. Pfahl, H. Wernli, Quantifying the relevance of atmospheric blocking for co-located temperature extremes in the Northern Hemisphere on (sub-)daily time scales. *Geophys. Res. Lett.* **39**, L12807 (2012).
- M. Luo, G. Ning, F. Xu, S. Wang, Z. Liu, Y. Yang, Observed heatwave changes in arid northwest China: Physical mechanism and long-term trend. *Atmos. Res.* **242**, 105009 (2020).
- M. Luo, X. Wang, N. Dong, W. Zhang, J. Li, S. Wu, G. Ning, L. Dai, Z. Liu, Two different propagation patterns of spatiotemporally contiguous heatwaves in China. *Science* **5**, 89 (2022).
- N. Schaller, J. Sillmann, J. Anstey, E. M. Fischer, C. M. Grams, S. Russo, Influence of blocking on Northern European and Western Russian heatwaves in large climate model ensembles. *Environ. Res. Lett.* **13**, 054015 (2018).
- P. A. Dirmeyer, G. Balsamo, E. M. Blyth, R. Morrison, H. M. Cooper, Land-atmosphere interactions exacerbated the drought and heatwave over Northern Europe during summer 2018. *AGU Adv.* **2**, e2020AV000283 (2021).
- D. G. Miralles, P. Gentile, S. I. Seneviratne, A. J. Teuling, Land-atmospheric feedbacks during droughts and heatwaves: State of the science and current challenges. *Ann. N. Y. Acad. Sci.* **1436**, 19–35 (2019).
- T. J. Parker, G. J. Berry, M. J. Reeder, The structure and evolution of heat waves in southeastern Australia. *J. Climate* **27**, 5768–5785 (2014).
- M. J. King, M. J. Reeder, Extreme heat events from an object viewpoint with application to south-east Australia. *Int. J. Climatol.* **41**, 2693–2709 (2021).
- M. Luo, N.-C. Lau, Summer heat extremes in northern continents linked to developing ENSO events. *Environ. Res. Lett.* **15**, 074042 (2020).
- B. Mueller, S. I. Seneviratne, Hot days induced by precipitation deficits at the global scale. *Proc. Natl. Acad. Sci.* **109**, 12398–12403 (2012).
- K. Wehrli, B. P. Guillod, M. Hauser, M. Leclair, S. I. Seneviratne, Identifying key driving processes of major recent heat waves. *J. Geophys. Res. Atmos.* **124**, 11746–11765 (2019).
- S. E. Perkins-Kirkpatrick, S. C. Lewis, Increasing trends in regional heatwaves. *Nat. Commun.* **11**, 3357 (2020).
- D. Luo, W. Zhang, L. Zhong, A. Dai, A nonlinear theory of atmospheric blocking: A potential vorticity gradient view. *J. Atmos. Sci.* **76**, 2399–2427 (2019).
- B. Luo, D. Luo, W. Zhuo, C. Xiao, A. Dai, I. Simmonds, Y. Yao, Y. Diao, T. Gong, Increased summer European heatwaves in recent decades: Contributions from greenhouse gases-induced warming and Atlantic multidecadal oscillation-like variations. *Earth's Future* **11**, e2023EF003701 (2023).
- D. Coumou, J. Lehmann, J. Beckmann, The weakening summer circulation in the Northern Hemisphere mid-latitudes. *Science* **348**, 324–327 (2015).
- Q. Tang, X. Zhang, J. A. Francis, Extreme summer weather in northern mid-latitudes linked to a vanishing cryosphere. *Nat. Clim. Change* **4**, 45–50 (2014).
- R. Dole, M. Hoerling, J. Perlwitz, J. Eischeid, P. Pegion, T. Zhang, X.-W. Quan, T. Xu, D. Murray, Was there a basis for anticipating the 2010 Russian heat wave? *Geophys. Res. Lett.* **38**, L06702 (2011).
- D. Coumou, V. Petoukhov, S. Rahmstorf, S. Petri, H. J. Schellnhuber, Quasi-resonant circulation regimes and hemispheric synchronization of extreme weather in boreal summer. *Proc. Natl. Acad. Sci. U.S.A.* **111**, 12331–12336 (2014).
- J. Lehmann, D. Coumou, The influence of mid-latitude storm tracks on hot, cold, dry and wet extremes. *Sci. Rep.* **5**, 17491 (2015).
- D. E. Horton, N. C. Johnson, D. Singh, D. L. Swain, B. Rajaratnam, N. S. Diffenbaugh, Contribution of changes in atmospheric circulation patterns to extreme temperature trends. *Nature* **522**, 465–469 (2015).
- S. F. Kew, S. Y. Philip, G. J. van Oldenborgh, G. van der Schrier, F. E. L. Otto, R. Vautard, The exceptional summer heat wave in southern Europe 2017. *Bull. Am. Meteorol. Soc.* **100**, S49–S53 (2019).
- S. E. Perkins-Kirkpatrick, P. B. Gibson, Changes in regional heatwave characteristics as a function of increasing global temperature. *Sci. Rep.* **7**, 12256 (2017).
- H. Hersbach, B. Bell, P. Berrisford, S. Hirahara, A. Horányi, J. Muñoz-Sabater, J. Nicolas, C. Peubey, R. Radu, D. Schepers, A. Simmons, C. Soci, S. Abdalla, X. Abellan, G. Balsamo, P. Bechtold, G. Biavati, J. Bidlot, M. Bonavita, G. De Chiara, P. Dahlgren, D. Dee, M. Diamantakis, R. Dragani, J. Flemming, R. Forbes, M. Fuentes, A. Geer, L. Haimberger, S. Healy, R. J. Hogan, E. Hólm, M. Janisková, S. Keeley, P. Laloyaux, P. Lopez, C. Lupu, G. Radnoti, P. de Rosnay, I. Rozum, F. Vamborg, S. Villaume, J.-N. Thépaut, The ERA5 global reanalysis. *Q. J. Roy. Meteorol. Soc.* **146**, 1999–2049 (2020).
- M. Kanamitsu, W. Ebisuzaki, J. Woollen, S.-K. Yang, J. J. Hnilo, M. Fiorino, G. L. Potter, NCEP–DOE AMIP-II Reanalysis (R-2). *Bull. Am. Meteorol. Soc.* **83**, 1631–1644 (2002).
- R. Gelaro, W. McCarty, M. J. Suárez, R. Todling, A. Molod, L. Takacs, C. A. Randles, A. Darmenov, M. G. Bosilovich, R. Reichle, K. Wargan, L. Coy, R. Cullather, C. Draper, S. Akella, V. Buchard, A. Conaty, A. M. da Silva, W. Gu, G.-K. Kim, R. Koster, R. Lucchesi, D. Merkova, J. E. Nielsen, G. Partyka, S. Pawson, W. Putman, M. Rienecker, S. D. Schubert,

- M. Sienkiewicz, B. Zhao, The modern-era retrospective analysis for research and applications, version 2 (MERRA-2). *J. Climate* **30**, 5419–5454 (2017).
47. G. S. Stipanuk, Algorithms for generating a skew-t, log p diagram and computing selected meteorological quantities (ed. Vol. Fort Monmouth, New Jersey, USA Army Electronics Command, 1973).
 48. J. Liu, J. Zhang, D. Kong, X. Feng, S. Feng, M. Xiao, Contributions of anthropogenic forcings to evapotranspiration changes over 1980–2020 using GLEAM and CMIP6 simulations. *J. Geophys. Res. Atmos.* **126**, e2021JD035367 (2021).
 49. S. Paik, S.-K. Min, X. Zhang, M. G. Donat, A. D. King, Q. Sun, Determining the anthropogenic greenhouse gas contribution to the observed intensification of extreme precipitation. *Geophys. Res. Lett.* **47**, e2019GL086875 (2020).
 50. B. C. O'Neill, C. Tebaldi, D. P. van Vuuren, V. Eyring, P. Friedlingstein, G. Hurtt, R. Knutti, E. Kriegler, J. F. Lamarque, J. Lowe, G. A. Meehl, R. Moss, K. Riahi, B. M. Sanderson, The scenario model intercomparison project (scenariomip) for CMIP6. *Geosci. Model Dev.* **9**, 3461–3482 (2016).
 51. W. Silversmith, <https://pypi.org/project/connected-components-3d/>, Ed. (2021), vol. 2021.
 52. S. Bathiany, V. Dakos, M. Scheffer, T. M. Lenton, Climate models predict increasing temperature variability in poor countries. *Sci. Adv.* **4**, eaar5809 (2018).
 53. L. Vogt, F. A. Burger, S. M. Griffies, T. L. Frölicher, Local drivers of marine heatwaves: A global analysis with an Earth system model. *Front. Clim.* **4**, 847995 (2022).
 54. S. Yue, C. Wang, The Mann-Kendall test modified by effective sample size to detect trend in serially correlated hydrological series. *Water Resour. Manag.* **18**, 201–218 (2004).
 55. R. M. Horton, J. S. Mankin, C. Lesk, E. Coffel, C. Raymond, A review of recent advances in research on extreme heat events. *Curr. Clim. Change Rep.* **2**, 242–259 (2016).
 56. V. Petoukhov, S. Petri, S. Rahmstorf, D. Coumou, K. Kornhuber, H. J. Schellnhuber, Role of quasiresonant planetary wave dynamics in recent boreal spring-to-autumn extreme events. *Proc. Natl. Acad. Sci.* **113**, 6862–6867 (2016).
 57. G. J. Boer, T. G. Shepherd, Large-scale two-dimensional turbulence in the atmosphere. *J Atmos. Sci.* **40**, 164–184 (1983).
 58. S. E. Perkins, A review on the scientific understanding of heatwaves—their measurement, driving mechanisms, and changes at the global scale. *Atmos. Res.* **164–165**, 242–267 (2015).
 59. D. Coumou, V. Petoukhov, A. V. Eliseev, Three-dimensional parameterizations of the synoptic scale kinetic energy and momentum flux in the Earth's atmosphere. *Nonlinear Processes Geophys.* **18**, 807–827 (2011).
 60. B. Wild, I. Teubner, L. Moesinger, R. M. Zotta, M. Forkel, R. van der Schalie, S. Sitth, W. Dorigo, VODCA2GPP—A new, global, long-term (1988–2020) gross primary production dataset from microwave remote sensing. *Earth Syst. Sci. Data* **14**, 1063–1085 (2022).
 61. H. Ritchie, P. Rosado, M. Roser, Energy Production and Consumption (Our World in Data, 2022); <https://ourworldindata.org/energy-production-consumption>.

Acknowledgments

Funding: This work is supported by the National Natural Science Foundation of China (42371028 and 41871029) and the National Key R&D Program of China (2019YFC1510400). The appointment of Z.L. is supported by the start-up funding (G0101000155) of the Hong Kong University of Science and Technology (Guangzhou). **Author contributions:** Conceptualization: M.L., T.P., W.Z., S.W., and G.N.-C.L. Methodology: M.L., T.P., W.Z., S.W., G.N.-C.L., and Z.L. Formal analysis: S.W., M.L., T.P., X.W., G.N., and T.O.C. Investigation: S.W., M.L., T.O.C., and Y.Y. Resources: M.L., G.N.-C.L., and T.O.C. Funding acquisition: M.L. Data curation: S.W., M.L., and T.O.C. Validation: S.W., X.W., M.L., and T.O.C. Supervision: M.L., T.P., G.N.-C.L., Z.L., and T.O.C. Software: S.W. and M.L. Project administration: M.L., T.P., G.N.-C.L., and T.O.C. Visualization: S.W., M.L., G.N.-C.L., and T.O.C. Writing—original draft: M.L. and S.W. Writing—review and editing: M.L., S.W., W.Z., T.P., G.N.-C.L., Z.L., X.W., G.N., and T.O.C.

Competing interests: The authors declare that they have no competing interests. **Data and materials availability:** All data used in this study are available online. The ERA5 data are downloaded from <https://cds.climate.copernicus.eu/cdsapp#!/dataset/reanalysis-era5-single-levels?tab=overview>. The MERRA2 data are available from https://disc.gsfc.nasa.gov/datasets/M2T1NXSLV_5.12.4/summary. The NCEP2 data are available through <https://psl.noaa.gov/data/gridded/data.ncep.reanalysis2.html>. The CMIP6 model simulations are available from <https://esgf-node.llnl.gov/search/cmip6/>. All data needed to evaluate the conclusions in the paper are present in the paper and/or the Supplementary Materials. The data of the heatwave metrics and source code used to perform the analyses and create publication figures can be accessed at a Zenodo repository (<https://doi.org/10.5281/zenodo.10463872>).

Submitted 4 October 2023

Accepted 26 February 2024

Published 29 March 2024

10.1126/sciadv.adl1598